

RESEARCH ARTICLE | JUNE 03 2025

Wafer-scale fabrication of temperature-compensated alkali vapor cells **FREE**

Yang Li ; Marlou R. Slot ; Matthew T. Hummon ; Susan Schima ; John Kitching  

 Check for updates

Appl. Phys. Lett. 126, 224001 (2025)

<https://doi.org/10.1063/5.0264409>



Articles You May Be Interested In

Locally sealed microfabricated vapor cells filled from an ex situ Cs source

Appl. Phys. Lett. (April 2025)

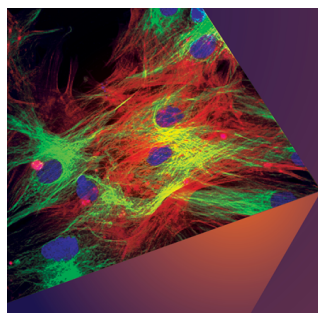
Chip-scale atomic devices

Appl. Phys. Rev. (August 2018)

Characterization of alkali-metal vapor cells fabricated with an alkali-metal source tablet

J. Vac. Sci. Technol. A (September 2016)

18 June 2025 17:34:50



Applied Physics Letters

Special Topics Open for Submissions

[Learn More](#)

Wafer-scale fabrication of temperature-compensated alkali vapor cells

Cite as: Appl. Phys. Lett. **126**, 224001 (2025); doi: [10.1063/5.0264409](https://doi.org/10.1063/5.0264409)

Submitted: 10 February 2025 · Accepted: 16 May 2025 ·

Published Online: 3 June 2025



View Online



Export Citation



CrossMark

Yang Li,^{1,2} Marlou R. Slot,^{1,2} Matthew T. Hummon,¹ Susan Schima,¹ and John Kitching^{1,a)}

AFFILIATIONS

¹Time and Frequency Division, National Institute of Standards and Technology, Boulder, Colorado 80305, USA

²Department of Physics, University of Colorado, Boulder, Colorado 80309, USA

^{a)}Author to whom correspondence should be addressed: john.kitching@nist.gov

ABSTRACT

We demonstrate wafer-scale fabrication of temperature-compensated alkali vapor cells using a mixture of Ar and N₂ buffer gases. The temperature coefficient of the fractional frequency shift of the hyperfine clock resonance is reduced from a typical value of $\approx 30 \times 10^{-9}/\text{K}$ for cells containing pure N₂ to below $\approx 3 \times 10^{-9}/\text{K}$ for the buffer gas mixture. This result is an important step toward the mass production of temperature-compensated atomic vapor cell-based devices such as chip-scale atomic clocks.

Published by AIP Publishing. <https://doi.org/10.1063/5.0264409>

Chip-scale atomic clocks (CSACs)^{1,2} are by now a successful commercial product and have been deployed in undersea seismic research,³ power grid applications,⁴ synchronization and time keeping in GPS-challenged environments,^{5,6} and space.⁷ CSACs achieve a long-term frequency stability superior to most quartz crystal and microelectromechanical systems (MEMS) oscillators, while maintaining a compact size and low power consumption.⁸ However, the relatively high cost of CSACs compared to most quartz oscillators, as well as low-volume manufacturing, impede their wider-spread use in real-world applications.

Microfabricated alkali vapor cells based on anodic bonding of glass and silicon⁹ are at the heart of CSACs, and wafer-level fabrication processes have been developed^{10–14} to enable low-cost, high-throughput manufacturing of CSACs and other atomic vapor cell-based sensors. Alkali atoms can be introduced into the cells using a variety of methods,^{9,15} including the chemical reactions of precursors,^{10,11,13,16,17} alkali dispenser pills,^{15,18,19} or the use of pure alkali metal,¹² which have all been demonstrated at the wafer level. In addition to the alkali atoms, atomic vapor cells in microwave clocks require a buffer gas to prevent wall-induced relaxation and enhance the quality factor of the microwave resonance in the clock. However, interactions between the alkali atoms and the buffer gas atoms introduce a temperature-dependent frequency shift of the hyperfine resonance.^{20,21} This temperature dependence is usually empirically described (in the absence of other frequency-changing perturbations) by a second-order polynomial,^{22,23}

$$\nu(T) = \nu_0 + P[\beta + \delta(T - T_0) + \gamma(T - T_0)^2], \quad (1)$$

where ν_0 is the unperturbed hyperfine splitting frequency of the alkali atom; $\nu(T)$ is the measured line-center frequency at temperature T , shifted from ν_0 due to collisions with buffer gases; P is the buffer gas pressure; and β , δ , and γ are the 0th-, 1st-, and 2nd-order coefficients for the temperature-dependent collisional shift specific to the type of buffer gas and alkali atoms.²¹ For cells containing a single gas species, the first-order term usually dominates, resulting in a frequency shift that is roughly linear in temperature to first order, but which may have a different sign depending on the buffer gas being used. By choosing a mixture of buffer gases with opposite first-order frequency shifts, the linear temperature coefficient can be reduced or canceled. Reduced temperature coefficients by optimizing buffer gas mixtures have been shown for individual Rb and Cs vapor cells with a Ne/Ar,^{24–27} Ar/N₂,²⁸ or He/Ne buffer gas mixtures.²⁹

The fabrication of temperature-compensated vapor cells at the wafer level is complicated by the way in which the alkali atoms are introduced to the cells. For example, cell-filling methods involving the dissociation of alkali azides after cell sealing^{9,30} create N₂ as a reaction product and achieving the correct buffer gas ratio requires stopping the dissociation reaction at a precise time or controlling precisely the quantity of initial reactants. On the other hand, methods that rely on the activation of an alkali molybdate Zr/Al pill¹⁵ typically getter N₂ during the activation;¹⁸ for this method a Ne/Ar mixture can be used for temperature compensation of Cs vapor cells.²⁵

Recently, we have developed a new process for producing micro-fabricated alkali vapor cells at the wafer scale.¹⁰ This process in principle enables the fabrication of wafers of vapor cells containing Rb or Cs

with any combination of buffer gases, or no buffer gases at all.¹³ Here, we show that this method is suitable for the production of temperature-compensated vapor cells. We fill an array of $1 \times 1 \times 1$ mm³ cells with an Ar/N₂ buffer gas mixture and demonstrate a reduced temperature coefficient (i.e., $\delta\nu(T)/\delta T$) for all vapor cells on the wafer by an order of magnitude over pure N₂ cells. The yield of functional vapor cells on the wafer is 64%.

Our wafer-scale cell fabrication process was described in detail in Refs. 10 and 13 and is shown here in Fig. 1(a). A 1 mm thick doped silicon wafer was etched using deep reactive ion etching with two spatially offset arrays of cavities as shown in Figs. 1(a) and 1(b): an array of optical cavities of area 1×1 mm², which will form the atomic vapor cells, and an array of auxiliary “deposition” cavities area of 0.75×0.75 mm², which contain the precursor materials needed to produce the alkali atoms. Long narrow channels were etched on the Si surface between the cavities to allow gases produced during the bonding process to escape.¹³

A 500 μ m thick borosilicate glass wafer was anodically bonded to one side of the Si wafer, forming the wafer preform. A precursor solution of BaN₆ and RbCl was then dispensed into the deposition cavities in the wafer preform using an automated syringe-based system. The wafer preform with precursors added was then loaded into a commercial wafer bonder, with a second 500 μ m thick borosilicate glass wafer located slightly above the open side of the Si wafer, and heated to 180 °C under vacuum. Metallic Rb was formed inside the deposition cavities by a chemical reaction of the precursor solution at this elevated temperature, which then evaporated and condensed on the lower surface of the top glass wafer due to the vertical temperature gradient. After cooling to 40 °C, the top glass wafer was lifted by a few millimeters and an Ar/N₂ buffer gas was introduced into the bonding chamber, resulting in a total chamber pressure of 749 mbar (562 Torr). This relatively high pressure was chosen for technical convenience to minimize arcing during the final anodic bonding step. The gas pressure ratio was adjusted to $P_{\text{Ar}} : P_{\text{N}_2} = 1.37:1$ following the experimental results in Ref. 22 to create a temperature-compensated buffer gas mixture with an expected turning point at 75 °C, at which $\delta\nu(T)/\delta T \approx 0$. We note that the measured turning point is higher than the expected value, around 100 °C, most likely due to N₂ generated from residual BaN₆ decomposition during the final anodic bonding step.

The top glass was then laterally translated to move the Rb droplets from the deposition cavities to the adjacent optical cavities and a final anodic bonding step was performed at 180 °C to create the final sealed atomic vapor cells. This relatively low temperature for anodic bonding was chosen to minimize Rb vapor leakage during the final bond while maintaining a good bonding quality. The fabricated wafer is displayed in Fig. 1(b), with the inset showing the individual atomic vapor cells containing Rb as well as the smaller deposition cavities.

After fabrication, the frequency of the ⁸⁷Rb $|^2S_{1/2}, F = 1, m_F = 0\rangle \rightarrow |^2S_{1/2}, F = 2, m_F = 0\rangle$ clock transition was measured for each cell on the wafer using coherent population trapping (CPT) excitation on the D1 line with a vertical cavity surface-emitting laser (VCSEL). This was carried out as a function of temperature between 88 and 108 °C in a magnetically shielded environment with an applied longitudinal field of $\approx 40 \mu T$. The VCSEL was modulated at one-half the hyperfine splitting frequency (about 3.417 GHz) using an RF synthesizer, which was referenced to a hydrogen maser. The light was circularly polarized after a quarter wave plate and its power was 1.2 μW before entering the cell with a beam $1/e^2$ radius of about 0.15 mm. The laser frequency detuning was optimized by tuning the laser frequency to a point near the bottom of the absorption profile to yield the highest signal-to-noise ratio (SNR) for the majority of cells, and subsequently the series of CPT measurements was performed without active wavelength stabilization. Autobalanced photodetection of the transmitted beam and a reference beam was used to adjust for the varying intensities of the transmitted power within the array of atomic vapor cells.

A typical CPT spectrum obtained with frequency modulated (FM) lock-in detection is shown in Fig. 2(a), acquired by stepping the RF synthesizer in a ± 20 kHz range around the estimated frequency of the CPT resonance. The full-width-half-maximum of the corresponding Lorentzian CPT line shape is around 3.6 kHz. To enhance the signal-to-noise ratio, we measured the lock-in signal at two frequencies near the center of CPT resonance and estimated the CPT center frequency from the two datapoints in real-time with a measurement time totaling 20–30 s per center frequency measured.

Figure 2(b) shows the measured CPT center frequency shift compared to the unperturbed hyperfine splitting of ⁸⁷Rb, $\nu(T) - \nu_0$, across the Ar/N₂ wafer measured at $T = (100 \pm 0.5)$ °C. Out of the total of nearly 26×17 cells etched on the wafer, only the 24×12 cells in the

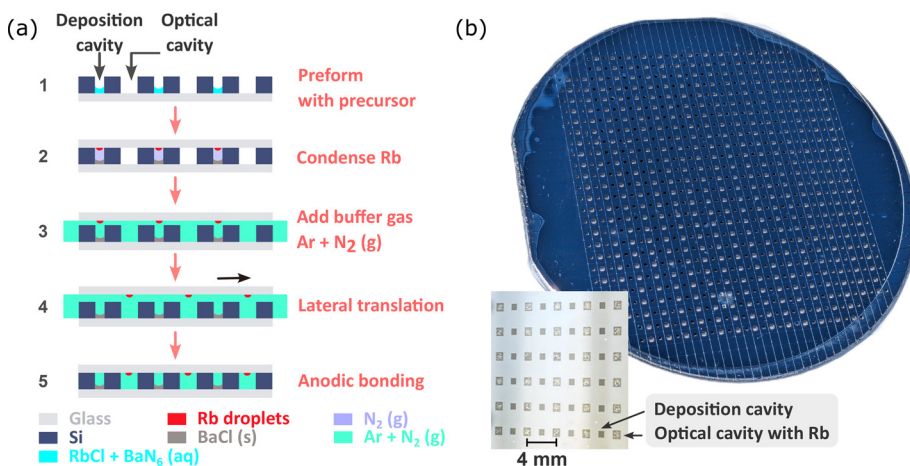


FIG. 1. (a) Wafer-scale fabrication process of alkali vapor cells with temperature-compensated buffer gas mixture. In step 3, the pressure ratio between Ar and N₂ is controlled to cancel the first-order CPT temperature coefficient. (b) Wafer after fabrication. Inset: magnified view of optical cavities containing Rb and the auxiliary deposition cavities.

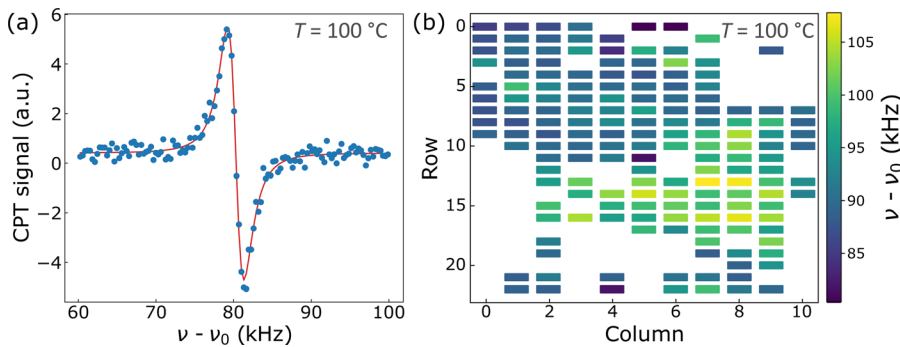


FIG. 2. (a) A sample CPT spectrum obtained by lock-in detection for a cell with Ar/N₂ buffer gas mixture at $T = (100 \pm 0.5)^\circ\text{C}$. The red curve represents a fit using the derivative of the Lorentzian function. (b) CPT center frequency shift across the wafer measured at $T = (100 \pm 0.5)^\circ\text{C}$. The row and column correspond to the wafer orientation in Fig. 1(b). A white region indicates the absence of Rb in the vapor cells.

center of the wafer were filled with chemical precursor, and of these, 23×11 cells were measured due to the limited range of the motorized stages that translated the cell wafer through the laser beam. 64% of the measured cells were found to be filled with Rb [colored boxes in Fig. 2(b)], which is a higher yield than reported previously for wafer-level fabrication using a precursor solution of BaN₆ and RbCl.^{10,13} The measured CPT center frequency has a spread of 27.4 kHz across the wafer. This spread is presumably caused by pressure variations due to BaN₆ decomposition in the final anodic bonding step.

The lower panel of Fig. 3(a) shows the temperature dependence of the CPT center frequency $\nu(T)$ for a cell (red) filled with 500 mbar (375 Torr) of pure N₂ buffer gas. For comparison, three cells from the wafer described above with 749 mbar (562 Torr) of Ar/N₂ mixture are displayed in the blue-shaded area. The temperature dependence of the cell with N₂ buffer gas is dominated by the first-order terms in Eq. (1) and shows a large temperature coefficient. In contrast, the buffer gas mixture clearly reduced the temperature coefficient compared to pure

N₂ cells, despite the 1.5 times higher total pressure in the cell. The upper panel of Fig. 3(a) shows an expanded view of the temperature-dependence curve of the three Ar/N₂ cells. For the majority of cells on the wafer, we measured a downward parabolic shape of the temperature curve, as shown by the blue data points in the upper panel of Fig. 3(a). However, some cells showed linear behavior (purple curve), abnormal patterns of oscillation or positive curvature; an example of the latter is shown by the green points in Fig. 3(a). Similar abnormal patterns have been reported by others previously.^{32–34} This anomalous temperature dependence is unlikely to be caused by the buffer gas collisional shift and its magnitude is consistent with light shifts measured by varying the laser power. We keep the light intensity as low as possible while still retaining acceptable signal-to-noise ratio in order to suppress the light shift, but its magnitude remains comparable to the temperature-induced variation in the buffer gas induced collisional shift in most of the cells. The light shift may be bigger in some cells [such as the one corresponding to the green data points in Fig. 3(a)]

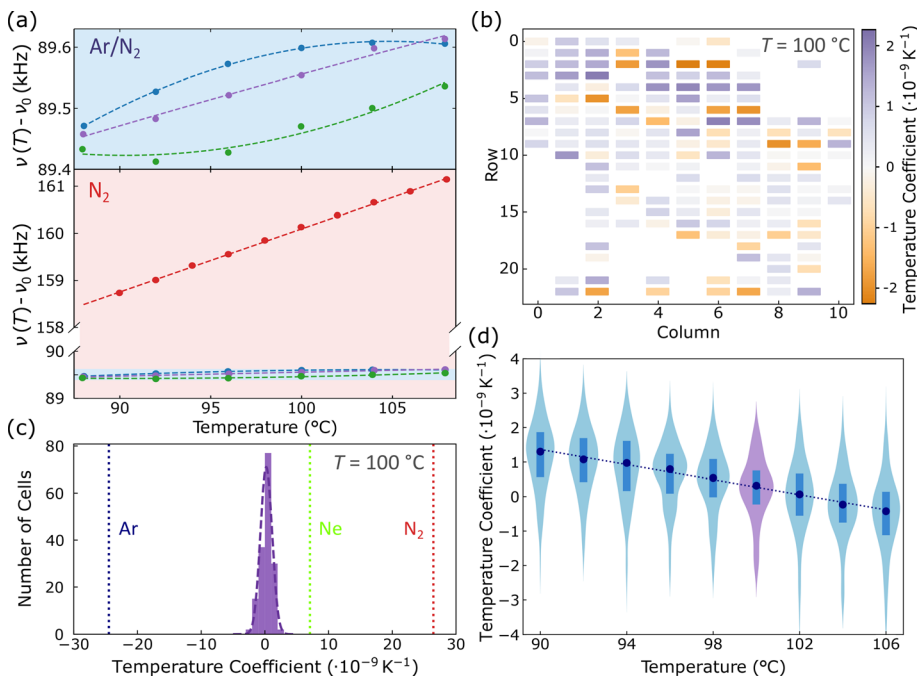


FIG. 3. (a) Comparison of the temperature-dependent CPT center frequency shift for three cells from a wafer filled with Ar/N₂ mixture (blue/purple/green data in top and bottom panel) and one cell from a wafer filled with pure N₂ (red data in bottom panel). The dashed lines are parabolic fits. The measured temperature coefficient of the N₂ cell (red) is around $1.9 \times 10^{-8} \text{ K}^{-1}$. The spread of the center frequency shift curves of the Ar/N₂-filled cells is more than 10 times smaller, despite the 1.5 times higher sealing pressure. (b) Spatial distribution of the temperature coefficients at $T = (100 \pm 0.5)^\circ\text{C}$ for all cells on the wafer. (c) Histogram of the temperature coefficients at $T = (100 \pm 0.5)^\circ\text{C}$ for all cells. The theoretical estimates²³ for pure Ar (blue), Ne (green),³¹ and N₂ (red) buffer gas at 100 °C are indicated for comparison. The purple dashed line indicates a Gaussian fit. (d) Violin plots showing the distribution of all temperature coefficients (blue/purple background), median (dot), and inter-quartile range (blue bar) as a function of temperature. The median values can be fitted linearly as a function of temperature (dotted line).

due to differences from cell to cell in transmitted intensity caused by Rb condensation on the window, magnetic field gradients from the heating wire and translation stage, spin-exchange broadening/shifts, or etalon effects. The chosen temperature range from 88 to 108 °C allows for a reasonable SNR while avoiding the spin-exchange broadening regime, which became noticeable in most cells above these temperatures. The temperature dependence for each column on the wafer was acquired over the course of 5 h per column. The temperature-dependent center frequency shifts were reproducible over this time period, implying that drift in the system (such as laser frequency drift) was small compared to the temperature-induced buffer gas induced collisional shift.

Next, we acquired the temperature dependence of the CPT center frequency for all measured cells on the wafer and derived the fractional temperature coefficients, $\frac{\Delta\nu(T)/\Delta T}{\nu_0}$. Figure 3(b) shows the temperature coefficients across the wafer at 100 °C, as determined from the slopes of the linear fits of the CPT center frequencies at 96, 100, and 104 °C. The values are within the range -2.2×10^{-9} to $+2.1 \times 10^{-9}/\text{K}$. Figure 3(c) displays the same temperature coefficients in a histogram. We fit the histogram to a Gaussian distribution, with a mean of $0.21 \times 10^{-9}/\text{K}$ and a standard deviation of $0.92 \times 10^{-9}/\text{K}$. Notably, all temperature coefficients are significantly smaller than the theoretical value for pure Ar, N₂, and Ne cells, as indicated by the dashed vertical lines at -24.5×10^{-9} , 26.5×10^{-9} , and $7.0 \times 10^{-9}/\text{K}$, respectively. These values were determined based on estimated temperature coefficients of Ar, N₂, and Ne, which were evaluated to be -0.45 , 0.49 , and $0.13 \text{ Hz K}^{-1} \text{ Torr}^{-1}$ at 100 °C using the coefficients in Ref. 23, and a conservative estimate of the sealing pressure of $P = 496 \text{ mbar}$ (372 Torr) at 300 K.

The distribution of temperature coefficients is reproduced at other temperatures, as visualized in the violin plots from 90 to 106 °C in Fig. 3(d). Importantly, the median values (blue dots) decrease linearly with temperature as indicated by the dashed line, crossing zero at 102.5 °C. This linear temperature dependence of the temperature coefficient corresponds to a parabolic temperature dependence of the median CPT center frequency with a turning point at 102.5 °C. This turning point temperature is somewhat above the expected value of 75 °C from the estimated gas pressure ratio, which can be explained by tens of Torr of N₂ being generated by the additional decomposition of BaN₆ decomposition during the final anodic bonding step. At each measured temperature, the semi-interquartile range is smaller than $0.7 \times 10^{-9}/\text{K}$ (blue bars), indicating that 50% of the buffer gas cells have a temperature coefficient that is at least 37 times lower than that for pure N₂ buffer gas at the zero-crossing temperature. The standard deviation is less than $1.1 \times 10^{-9}/\text{K}$ at all temperatures, with 73% of the cells having a reduced temperature coefficient by at least 24 times compared to pure N₂ buffer gas at the zero-crossing temperature. We note that this standard deviation and the average measured turning point remain similar if only the majority of 80% of cells that can be fitted with a downward (as opposed to 20% with an upward) parabola are considered. The results show that all cells containing a mixture of Ar and N₂ buffer gases have substantially reduced temperature coefficients compared to the conservative estimates for pure buffer gases. It should be noted that the distributions of temperature coefficients in Figs. 3(c) and 3(d) are also impacted by effects unlikely to be related to buffer gas collisions, as discussed above. We therefore expect that the temperature coefficients due to buffer gas collisions alone will have a smaller variance than the measurements here indicate.

In summary, we demonstrated a wafer-scale fabrication and characterization process that is capable of producing temperature-compensated alkali vapor cells using a mixture of Ar and N₂ buffer gases. The buffer gas mixture reduced the temperature coefficient of the clock resonance frequency by at least an order of magnitude compared to pure N₂ buffer gas. The yield of the wafer was 64%. The described wafer-scale results pave the way for low-cost CSACs with increased temperature stability.

The authors thank Argyrios Dellis, Robert Compton, William McGehee, Ying-Ju Wang, Daniel Slichter, Mario Maldonado, and Yifan Liu for helpful discussions.

AUTHOR DECLARATIONS

Conflict of Interest

The authors have no conflicts to disclose.

Author Contributions

Yang Li: Conceptualization (equal); Formal analysis (equal); Investigation (lead); Methodology (equal); Resources (equal); Software (equal); Validation (equal); Visualization (equal); Writing – original draft (lead); Writing – review & editing (equal). **Marlou R. Slot:** Conceptualization (equal); Formal analysis (equal); Funding acquisition (equal); Investigation (equal); Methodology (equal); Software (equal); Validation (equal); Visualization (lead); Writing – original draft (equal); Writing – review & editing (equal). **Matthew T. Hummon:** Resources (equal); Supervision (supporting); Writing – review & editing (equal). **Susan Schima:** Investigation (supporting); Resources (equal). **John Kitching:** Conceptualization (lead); Formal analysis (equal); Funding acquisition (lead); Investigation (supporting); Methodology (equal); Project administration (lead); Resources (lead); Supervision (lead); Validation (equal); Writing – original draft (equal); Writing – review & editing (equal).

DATA AVAILABILITY

The data that support the findings of this study are available from the corresponding author upon reasonable request.

REFERENCES

- S. Knappe, V. Shah, P. D. Schwindt, L. Hollberg, J. Kitching, L.-A. Liew, and J. Moreland, "A microfabricated atomic clock," *Appl. Phys. Lett.* **85**, 1460–1462 (2004).
- R. Lutwak, D. Emmons, T. English, W. Riley, A. Duwel, M. Varghese, D. Serkland, and G. Peake, "The chip-scale atomic clock - recent development progress," in *Proceedings of the 35th Annual Precise Time and Time Interval Systems and Applications Meeting* (Institute of Navigation, 2003), pp. 467–478.
- A. T. Gardner and J. A. Collins, "A second look at chip scale atomic clocks for long term precision timing," in *OCEANS 2016 MTS/IEEE Monterey* (IEEE, 2016), pp. 1–9.
- L. Zhan, Y. Liu, W. Yao, J. Zhao, and Y. Liu, "Utilization of chip-scale atomic clock for synchrophasor measurements," *IEEE Trans. Power Delivery* **31**, 2299–2300 (2016).
- E. Fernández, D. Calero, and M. E. Parés, "CSAC characterization and its impact on GNSS clock augmentation performance," *Sensors* **17**, 370 (2017).
- L. Ma, Z. You, T. Liu, and S. Shi, "Coupled integration of CSAC, MIMU, and GNSS for improved PNT performance," *Sensors* **16**, 682 (2016).
- T. Ely, Z. Towfic, and D. Sorensen, "Formulation and characterization of one-way radiometric tracking with the iris radio using a chip-scale atomic clock," *NAVIGATION* **71**, navi.633 (2024).

- ⁸J. Kitching, “Chip-scale atomic devices,” *Appl. Phys. Rev.* **5**, 031302 (2018).
- ⁹L.-A. Liew, S. Knappe, J. Moreland, H. Robinson, L. Hollberg, and J. Kitching, “Microfabricated alkali atom vapor cells,” *Appl. Phys. Lett.* **84**, 2694–2696 (2004).
- ¹⁰D. Bopp, V. Maurice, and J. Kitching, “Wafer-level fabrication of alkali vapor cells using in-situ atomic deposition,” *J. Phys. Photonics* **3**, 015002 (2021).
- ¹¹P. Guo, H. Meng, L. Dan, and J. Zhao, “Wafer-level filling of mems vapor cells based on chemical reaction and evaporation,” *Micromachines* **13**, 217 (2022).
- ¹²P. Guo, H. Meng, L. Dan, and J. Zhao, “Wafer-level assembly of physics package for chip-scale atomic clocks,” *IEEE Sens. J.* **22**, 6387–6398 (2022).
- ¹³Y. Li, D. B. Sohn, M. T. Hummon, S. Schima, and J. Kitching, “Wafer-scale fabrication of evacuated alkali vapor cells,” *Opt. Lett.* **49**, 4963–4966 (2024).
- ¹⁴T. Overstolz, J. Haesler, G. Bergonzi, A. Pezous, P.-A. Clerc, S. Ischer, J. Kaufmann, and M. Despont, “Wafer scale fabrication of highly integrated rubidium vapor cells,” in *2014 IEEE 27th International Conference on Micro Electro Mechanical Systems (MEMS)* (IEEE, 2014), pp. 552–555.
- ¹⁵L. Nieradko, C. Gorecki, A. Douahi, V. Giordano, J. C. Beugnot, J. Dziuban, and M. Moraja, “New approach of fabrication and dispensing of micromachined cesium vapor cell,” *J. Micro/Nanolithogr. MEMS MOEMS* **7**, 033013 (2008).
- ¹⁶T. Dyer, S. Ingleby, C. Dunare, K. Dodds, P. Lomax, P. Griffin, and E. Riis, “Micro-fabricated caesium vapor cell with 5 mm optical path length,” *J. Appl. Phys.* **132**, 204401 (2022).
- ¹⁷S. Karlen, J. Gobet, T. Overstolz, J. Haesler, and S. Lecomte, “Lifetime assessment of RbN₃-filled MEMS atomic vapor cells with Al₂O₃ coating,” *Opt. Express* **25**, 2187–2194 (2017).
- ¹⁸S. Dyer, A. McWilliam, D. Hunter, S. Ingleby, D. Burt, O. Sharp, F. Mirando, P. Griffin, E. Riis, and J. McGilligan, “Nitrogen buffer gas pressure tuning in a micro-machined vapor cell,” *Appl. Phys. Lett.* **123**, 074001 (2023).
- ¹⁹V. Maurice, C. Carlé, S. Keshavarzi, R. Chutani, S. Queste, L. Gauthier-Manuel, J.-M. Cote, R. Vicarini, M. Abdel Hafiz, R. Boudot *et al.*, “Wafer-level vapor cells filled with laser-actuated hermetic seals for integrated atomic devices,” *Microsyst. Nanoeng.* **8**, 129 (2022).
- ²⁰B. Bean and R. Lambert, “Temperature dependence of hyperfine density shifts. III. ²³Na, ³⁹K, and ⁸⁵Rb in He, Ne, Ar, and N₂,” *Phys. Rev. A* **12**, 1498 (1975).
- ²¹J. Vanier and C. Audoin, *The Quantum Physics of Atomic Frequency Standards* (CRC Press, 1989).
- ²²J. Vanier, R. Kunski, N. Cyr, J. Savard, and M. Têtu, “On hyperfine frequency shifts caused by buffer gases: Application to the optically pumped passive rubidium frequency standard,” *J. Appl. Phys.* **53**, 5387–5391 (1982).
- ²³L.-C. Ha, X. Zhang, N. Dao, and K. R. Overstreet, “D1 line broadening and hyperfine frequency shift coefficients for ⁸⁷Rb and ¹³³Cs in Ne, Ar, and N₂,” *Phys. Rev. A* **103**, 022826 (2021).
- ²⁴R. Boudot, D. Miletic, P. Dziuban, C. Affolderbach, P. Knapkiewicz, J. A. Dziuban, G. Mileti, V. Girodano, and C. Gorecki, “First-order cancellation of the Cs clock frequency temperature-dependence in Ne-Ar buffer gas mixture,” *Opt. Express* **19**(4), 3106–3114 (2011).
- ²⁵R. Boudot, P. Dziuban, V. Giordano, C. Gorecki, D. Miletic, C. Affolderbach, G. Mileti, P. Knapkiewicz, and J. A. Dziuban, “Cs collisional frequency shift measurements in microcells filled with a Ne-Ar buffer gas mixture,” *2011 Joint Conference of the IEEE International Frequency Control and the European Frequency and Time Forum (FCS) Proceedings* (IEEE, 2011), pp. 1–3.
- ²⁶K. Deng, T. Guo, D. W. He, X. Y. Liu, L. Liu, D. Z. Guo, X. Z. Chen, and Z. Wang, “Effect of buffer gas ratios on the relationship between cell temperature and frequency shifts of the coherent population trapping resonance,” *Appl. Phys. Lett.* **92**, 211104 (2008).
- ²⁷K. Deng, X. Chen, and Z. Wang, “Minimization of the temperature coefficient of resonance frequency shift in the coherent population trapping clock,” *Opt. Lett.* **36**, 1740–1742 (2011).
- ²⁸O. Kozlova, S. Guérandel, and E. de Clercq, “Temperature and pressure shift of the Cs clock transition in the presence of buffer gases: Ne, N₂, Ar,” *Phys. Rev. A* **83**, 062714 (2011).
- ²⁹E. Kroemer, M. Abdel Hafiz, V. Maurice, B. Fouilland, C. Gorecki, and R. Boudot, “Cs vapor microcells with Ne – He buffer gas mixture for high operation-temperature miniature atomic clocks,” *Opt. Express* **23**, 18373–18380 (2015).
- ³⁰S. Woetzel, V. Schultze, R. Ijsselsteijn, T. Schulz, S. Anders, R. Stolz, and H. G. Meyer, “Microfabricated atomic vapor cell arrays for magnetic field measurements,” *Rev. Sci. Instrum.* **82**, 033111 (2011).
- ³¹The presence of Ne as a buffer gas produces a non-zero temperature coefficient for Rb at temperatures below 150 °C, but we note that Ne produces a turning point near 80 °C for Cs. See, for example, O. Kozlova, R. Boudot, S. Guérandel, and E. de Clercq, “Temperature dependence cancellation of the Cs clock frequency in the presence of Ne buffer gas,” *IEEE Trans. Instrum. Meas.* **60**, 2262–2266 (2011).
- ³²S. Karlen, “Fabrication and characterization of MEMS alkali vapor cells used in chip-scale atomic clocks and other atomic devices,” Ph.D. thesis (Université de Neuchâtel, 2017).
- ³³D. Miletic, “Light-shift and temperature-shift studies in atomic clocks based on coherent population trapping,” Ph.D. thesis (University of Neuchâtel, 2013).
- ³⁴Y. Masian, A. Sivak, D. Sevostianov, V. Vassiliev, and V. Velichansky, “Study and optimization of CPT resonance parameters in ⁸⁷Rb/Ar/Ne microcells aimed for application in metrology,” *Phys. Proc.* **71**, 252–256 (2015).